

Topologically customized and surface-mounted meta-devices for Lamb wave manipulation

Ze Liu^{1,2} , Sheng-Bo Shan³ , Hao-Wen Dong⁴ and Li Cheng^{1,2,5,*} 

¹ Department of Mechanical Engineering, The Hong Kong Polytechnic University, Kowloon, Hong Kong

² The Hong Kong Polytechnic University Shenzhen Research Institute, Shenzhen 518057, People's Republic of China

³ School of Aerospace Engineering and Applied Mechanics, Tongji University, Shanghai 200092, People's Republic of China

⁴ Institute of Advanced Structure Technology, Beijing Institute of Technology, Beijing 100081, People's Republic of China

⁵ The Hong Kong Branch of National Rail Transit Electrification and Automation Engineering Technology Research Center, The Hong Kong Polytechnic University, Kowloon, Hong Kong

E-mail: li.cheng@polyu.edu.hk

Received 14 January 2022, revised 25 March 2022

Accepted for publication 6 April 2022

Published 20 April 2022



CrossMark

Abstract

Lamb waves inside thin-walled structures have received extensive attention due to their great promise in applications such as structural health monitoring. Applications point at the common need for effective conditioning and manipulation of the wave propagation in terms of both frequency content and mode components. In this work, the concept of metamaterials is exploited to construct functional meta-devices (MDs). The MDs are designed to deliver prescribed functionalities after they are surface-mounted onto a structure conveying Lamb waves. To this end, a unified inverse-design scheme based on topology optimization is proposed and applied to achieve multifold functions such as frequency filtering, single-mode transmission and wave filtering at the subwavelength scale. Configuration features of the optimized MDs are extracted to reveal the mechanism governing the generation of broad Bragg scattering bandgaps. Analyses on negative effective mass density and the polarized mode explain the directional locally resonant bandgaps which exhibit strong anisotropic density. A representative MD with a finite number of unit cells is examined through finite element simulations. Temporal signals and their transmission spectra confirm the expected band features. An experiment is carried out to confirm the prescribed wave manipulation functions of the designed MD in terms of achieving selective frequency and wave mode transmission. This work provides a universal approach for topologically customizing MDs for the precise and tactic control of Lamb wave propagation.

Keywords: guided wave, metamaterial, topology optimization, wave filter, structural health monitoring

(Some figures may appear in colour only in the online journal)

* Author to whom any correspondence should be addressed.

1. Introduction

Ultrasonic guided waves, especially Lamb waves, have received increasing attention due to their appealing advantages like low energy consumption, long propagation distance and high sensitivity to structural damages. These properties triggered vast engineering applications, exemplified by the structural health monitoring (SHM) [1, 2]. In this particular context, especially for nonlinear wave based methods [3–6], there exist some bottlenecks which impede the practical feasibility of the detection methods. While recognizing their enhanced sensitivity to damage, numerous adverse factors may affect the extraction of damage information, deteriorate the detection accuracy or even jeopardize the entire SHM process. On the top of the list, one can name the undesired wave distortion caused by transducers, installation adhesives and measurement equipment, etc [7]. Meanwhile, the signal complexity, due to the co-existence of multiple wave modes and the undesired frequency components, is also seen as another major problem. This poses a harsh demand on the probing signals and hatches out the need for their meticulous control and manipulation. In addition to a careful system design [8–10], effective wave manipulation, allowing for targeted frequency selection and selective mode transmission, is highly desirable. From a broader perspective, the problem raised above is generic in nature, falling into the general category of Lamb wave manipulation which is relevant to a large class of engineering problems.

The aforementioned task can be materialized by embracing the concept of metamaterials. Metamaterial is a type of artificial composite structure/material that offers enormous possibilities for manipulating wave propagation properties, so as to deliver extraordinary wave functionalities like energy attenuation [11, 12], subwavelength imaging [13, 14], negative refraction [15, 16], non-reciprocity [17], phase modulation [18] and cloaking [19], etc. As one of the basic characteristics of metamaterials, bandgap [20–24], in which the propagation of specific-frequency waves is prohibited, shows great promise for wave filtering. Preliminary attempts have been made to explore this property for guided wave control. Some applications, exemplified by SHM, only allow metamaterial components to be surface-mounted [25, 26] to ensure the integrity of the structure under inspection, as opposed to the conventional and widely explored metamaterials with perforation or insertion in the structures/materials themselves [27, 28]. This hatched out the design of a few pillared-type metamaterials. For example, Tian *et al* [29, 30] utilized the aluminum-lead composite structures to respectively achieve the mitigation for deceptive secondary waves and the selective mode transmission. However, their design requires a meticulous installation of several stubs. As an improvement, Shan *et al* [31] proposed a metamaterial filter design with a flat base to connect the scatters. With a double-sided bonding of the metamaterial filters onto a plate, they improved the detection capacity of the SHM technique for the monitoring of micro-structural changes inside the plate. Although wave filtering and selective bandgap have been achieved by these existing

designs, most of them originate from empirical and intuitive designs with predefined structural configurations followed by tedious parameter tuning. In addition, to cope with more specific and higher-level demands, it will be extremely difficult, if not impossible, to follow the empirical metamaterial design approach. These challenges call for a systematic inverse-design strategy to tailor-make the property of metamaterials on demand.

In this study, we propose a unified inverse-design framework based on topology optimization to tactically design functional metamaterial devices, called meta-devices (MDs), for Lamb wave manipulation. The customized single-side and single-phase MDs are expected to deliver broadband wave manipulation functionalities including selective frequency filtering, single-mode transmission and low-frequency bandgaps. Note that, although most of the prescribed wave manipulation functionalities are inspired from SHM-specific requirements, the design method, as well as the associated tools developed in this work, is generic in nature, which can be extended to a much wider scope of applications. The configurational features of the optimized structures are extracted and scrutinized to shed light on the generation mechanisms of the broad bandgaps arising from Bragg scattering or local resonances. Both numerical and experimental studies are conducted to confirm the efficacy of a representative MD in terms of expected guided wave manipulation functions.

The remaining parts of this paper are organized as follows. Section 2 elaborates the wave manipulation needs, based on which the topology optimization framework is established for the customization design of MDs. Targeting these functions, optimization results are shown and discussed in section 3. The efficacy of the designed structures is then assessed from finite element simulations and experiments in section 4. Finally, section 5 summarizes the main contributions and conclusions of this study.

2. An inverse-design framework based on topology optimization

Embracing the concept of metamaterials, MDs are designed and surface-mounted onto a structure for manipulating the propagation of different Lamb wave components with required wave properties. It is important to reiterate that, compared with the perforation- or insertion-based metamaterials where the destructive interference for guided waves might more easily happen through the metamaterials themselves, the add-on MD design is technically more challenging since the expected effects can only be generated through the coupling of guided wave modes and stub modes arising from the MD.

As shown in figure 1(a), an MD comprises an array of periodically arranged elements (called unit cells), to be mounted on the surface of a structure under inspection. The proposed inverse strategy for the design of the unit cell based on topology optimization is established as illustrated in figures 1(b) and (c). The design domain of the MD is discretized into $m \times m$ binary pixels, where numbers represent different materials.

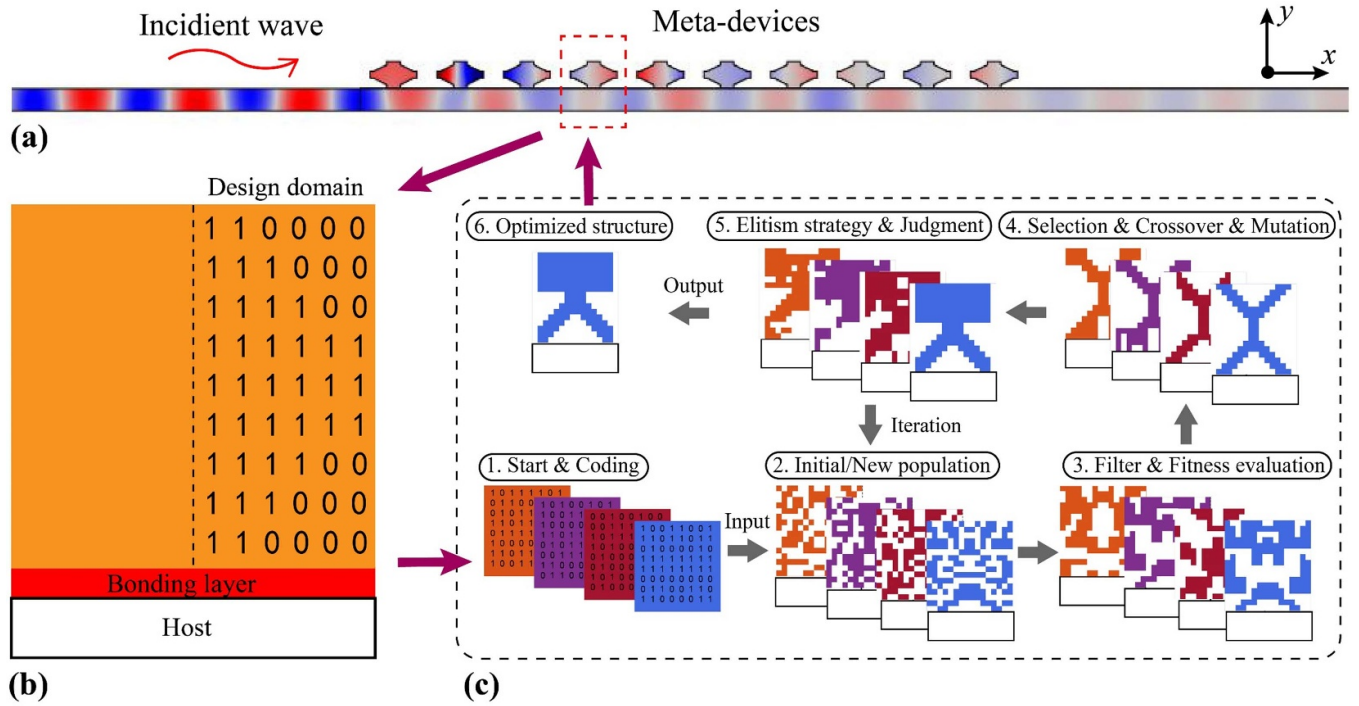


Figure 1. Schematic of the inversely designed meta-devices. (a) The wave filtering phenomenon induced by surface-mounted meta-devices, (b) the unit cell, including the host structure, the adhesive bonding layer and the design domain represented by a ‘0’ (for vacuum) and ‘1’ (for solid) matrix. (c) The topology optimization flowchart.

Targeting different frequency bands for different wave manipulation purposes as detailed later, the design objective is to maximize the bandgap width to obtain broadband functional MDs. The objective functions are generally formulated as:

$$\text{Find : } \theta_n = 0 \text{ or } 1, \quad (1)$$

$$\text{Maximize : } F_i = \max(\Omega_i^{\text{stop}}) - \min(\Omega_i^{\text{stop}}) \quad (2)$$

$$\text{Subject to : } k = [0, \pi/a], \quad (3)$$

$$\min : d(\Sigma) \geq d_1, \quad (4)$$

$$N(\Sigma) = N_1 \quad (5)$$

where θ_n denotes the value selection of the n th pixel in the entire $m \times m$ matrix, in which ‘1’ represents a solid material and ‘0’ for the vacuum; Ω_i^{stop} represents the set of the stop bands associated with the i th specific objective; a is the periodic constant; equation (4) states that the minimum size of the geometric feature should be larger than the prescribed value d_1 , which is set to $a/16$. Equation (5) limits the total number of the blocks within the design domain to $N_1 = 1$, so as to facilitate the sample fabrication and implementation.

Three typical cases are discussed to further explain the proposed inverse-design framework for Lamb wave customization. The rationale behind the selected objectives is substantiated using SHM as an example, while noting that

more diversified objectives could also be defined by following similar methodology.

Objective 1: A broadband selective frequency filter. For a given frequency excitation in an SHM system, the generated waves may contain other frequency components due to the wave distortion associated with the measurement system or transducers. These unexpected frequency components can adversely increase the signal complexity, interfere with damage-related signals or even put the damage identification into jeopardy. For example, in a nonlinear-guided-wave-based SHM system, the second harmonic waves induced by the non-damage-related sources may overwhelm the damage-related information. Therefore, a wave filter can be desired to tactically eliminate these undesired frequency components. In this case, the MDs should allow the passing of the desired-frequency waves while stopping the undesired-frequency components. This is mathematically defined as

$$\Omega_1^{\text{stop}} = \{ \{ \Omega^{\text{stop}} \} \cap (f_L^{\text{stop}}, f_U^{\text{stop}}) \} \cup \{ \{ \Omega^{\text{pass}} \} \cap (f_L^{\text{pass}}, f_U^{\text{pass}}) \} \quad (6)$$

where Ω^{stop} denotes the set of the stop bands while Ω^{pass} for the pass bands; f_L^{stop} and f_U^{stop} are the lower and upper edges of the constrained stop band range, respectively; f_L^{pass} and f_U^{pass} are the lower and upper edges of the constrained pass band range, respectively.

Objective 2: A broadband single-mode (symmetric or anti-symmetric Lamb wave mode) transmission filter. Multiple wave modes, including symmetric (S) and antisymmetric (A) Lamb modes, simultaneously exist, which increases the signal

complexity and hampers the effective extraction of the useful damage information during signal processing. In this case, a single-mode (S or A) transmission filter is desired to create a pass band with a single mode whilst stopping the other. This can be formulated as

$$\Omega_2^{\text{stop}} = \left\{ \left\{ \Omega_{\text{single}}^{\text{pass}} \right\} \cap (f_L^{\text{pass}}, f_U^{\text{pass}}) \right\} \quad (7)$$

where $\Omega_{\text{single}}^{\text{pass}}$ denotes the set of the single-mode pass bands (A or S mode).

Objective 3: broadband low-frequency filters. The lowest-order Lamb waves (S0 and A0 modes) in the low-frequency region are widely used in the SHM technique [8, 10, 32]. However, it is challenging to manipulate these low-frequency waves using reasonably small-size structures due to the long wavelengths of the probing waves. A proper MD might deliver low-frequency (subwavelength-scale) filtering with a prescribed geometric size. This is mathematically casted as

$$\Omega_3^{\text{stop}} = \left\{ \left\{ \Omega^{\text{stop}} \right\} \cap (0, f_U^{\text{stop}}) \right\}. \quad (8)$$

To yield the optimal MD configuration which satisfies the above requirements, either separately or concurrently, the key is to calculate and evaluate the objective functions in terms of the dispersion relations. This is realized with finite element simulations using COMSOL Multiphysics 5.2a. In light of the periodic arrangement of the MDs, a unit cell is extracted and shown in figure 1(b) which is composed of the portion of the host plate, an adhesive bonding layer and the added-on stub. The host plate and the adhesive layer are meshed into 10 and 5 layers along the thickness direction, respectively, and both 48 layers (associated with the following optimization setup) along the horizontal wave propagation direction. The design domain is discretized into triangular meshes. The Bloch-Floquet periodic conditions are applied to the left and right boundaries of the unit cell with other boundaries being set free. The dispersion relations can be calculated accordingly.

Genetic algorithm (GA) [33] is employed as the searching method for updating design variables. As illustrated in figure 1(c), the GA-based topological inverse-design scheme involves the following steps. An initial population P comprising M individuals is randomly generated first. Then, a graphical filtering processing including the abuttal entropy method [34] is conducted. After that, the objective functions of all individuals based on equation (2), in conjunction with equations (6)–(8), are calculated. Genetic operations including the linear selection, uniform crossover with the probability P_c and uniform mutation with the probability P_m are further performed to update design variables. The elitism strategy is applied to the new population. The termination criteria, like a prescribed cycle time or convergence standard, are judged. If met, the optimized structure is output; otherwise, the graphical processing step needs to be recalled to start the next generation. The procedural detail is readily available in the literature [23, 34].

Table 1. The material parameters.

	Density (kg m^{-3})	Poisson's ratio	Young's modulus (GPa)
Aluminum	2700	0.33	70
Adhesive	1080	0.4	1.31
Lead	11 600	0.369	40.8

It is relevant to note that the structural connectivity along the height direction (y direction) within the design domain is not required in the optimization process. Since any structural elements which completely disconnect with the continued base structure will not affect the bandgaps and dispersion calculations, they will also be considered obsolete in the formation of the MD element. As a result, the height of the optimized MD may not reach the top of the design domain.

3. Optimization results and discussions

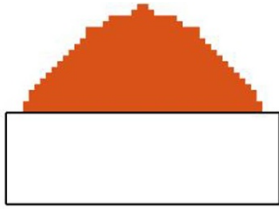
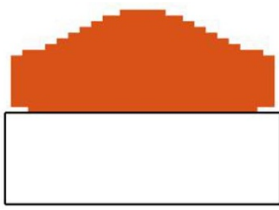
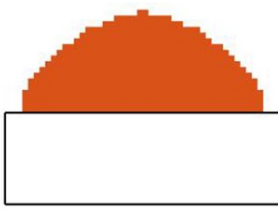
The GA parameters used in the proposed framework are defined as follows: the population size M is 30; the design domain is discretized into 48×48 pixels; the crossover and mutation probabilities are respectively set as 0.9 and 0.02. In the unit cell, the periodic constant is 6 mm. The host structure is a 2 mm thick aluminum plate. The surface-mounted MDs within a $6 \text{ mm} \times 6 \text{ mm}$ design domain use aluminum for objectives 1 and 2, and lead for objective 3 respectively as representative cases. The adhesive bonding layer is 0.05 mm thick. The involved material parameters are listed in table 1. Optimizations on the three aforementioned objectives are conducted using COMSOL Multiphysics 5.2a and MATLAB on a Windows cluster computer with two Intel Xeon Scalable Gold 6248R CPU @3.0 GHz. Each optimization procedure runs for around 25 h.

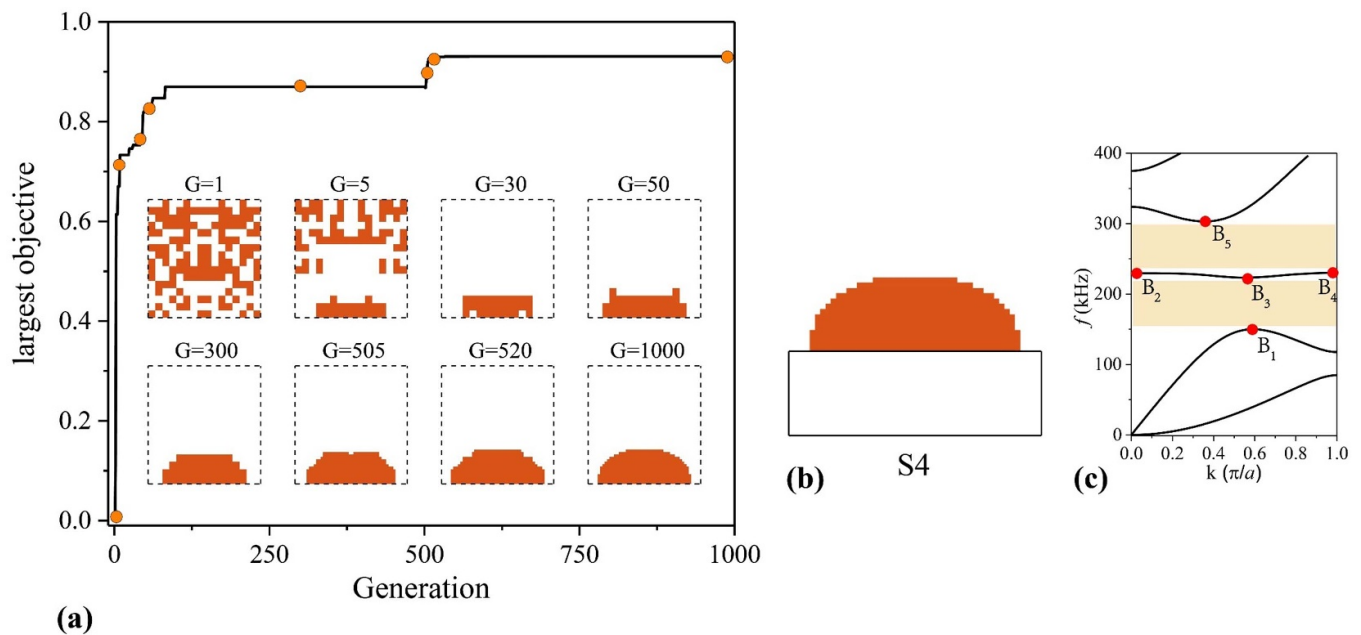
Before addressing the specific design of the predefined functional MDs, preliminary optimization attempts are conducted to examine the bandgap features in a general case. First, we define the bandgap between the j th and the $(j + 1)$ th band branches as the j th bandgap. Without imposing any constraints on the frequency or wave mode, the optimization objectives are set as the maximum width of the 2nd bandgap, the 3rd bandgap and their total (the 2nd and 3rd) bandgaps respectively. Table 2 exhibits the optimized structures and their broad bandgap positions. The widths of the 2nd and the 3rd bandgaps are both around 79 kHz and the total bandgap width reaches 152 kHz. It can also be observed that the bandgap range is mainly located at 150–300 kHz. These results demonstrate the effectiveness of the proposed topological design framework, while offering useful guidance to the subsequent SHM-specific MD design.

3.1. Selective frequency filters

In this case, the MDs are designed to deliver selective frequency wave transmission and prohibition. As in a typical nonlinear-guided-wave-based SHM system, the designed

Table 2. Optimization results aiming at maximum bandgap (BG) widths.

Optimization target	The 2nd BG	The 3rd BG	The total BG (2nd and 3rd)
Optimized structures			
BG regions (kHz)	S1 147.5~226.5	S2 206.9~286.1	S3 145.4~223.5 226.0~300.6

**Figure 2.** Optimization results aiming at the maximum selective-frequency bandgap widths in the SHM-specific frequency (200–300 kHz) region (objective 1). (a) The evolution histories, (b) the optimized structures and (c) the corresponding dispersion relations.

MDs are expected to allow the passing of the fundamental frequency wave whilst simultaneously filtering out its undesired second harmonic waves. In this case, strong probing waves at the fundamental frequency are required whilst the second harmonic components from the actuation part should be minimized so that the second harmonic signals captured outside the actuation area would only be attributed to the material nonlinearity of distributed material defects [35, 36]. As a representative example, a bandgap is customized in the range of 200–300 kHz, which is the second harmonic range corresponding to a fundamental frequency within 100–150 kHz. Deploying the established optimization procedure, the optimization results are shown in figure 2. The evolution process is illustrated in figure 2(a) with some representative intermediary configurations listed. It is observed that the evolution curve of the objective values increases dramatically at the early stage of the iteration and keeps almost flat at the late stage. This indicates that the proposed scheme can quickly discern the suitable structures and maintain stable convergence eventually. The finally

optimized MD is presented in figure 2(b) with its corresponding dispersion relations shown in figure 2(c). Visually, the add-on MD cell is composed of a single-block trapezoid-like stub. This relatively regular shape is conducive to fabrication and implementation. Most importantly, ultra-broad bandgaps amounting to 93.1 kHz wide are achieved within the targeted 100 kHz range.

3.2. Single-mode transmission filters

To further improve the functions of the MDs on the basis of the properties previously achieved in section 3.1, the single-mode transmission function of Lamb waves is added to reduce the signal complexity. This is exemplified by the passing of single S0-mode wave. Based on the frequency pairing requirement described in section 3.1, namely the passing of fundamental wave and the prohibition of its second harmonic wave, the widest passing band for S0 mode only, is set as the objective. Following the same procedure, the optimized structure

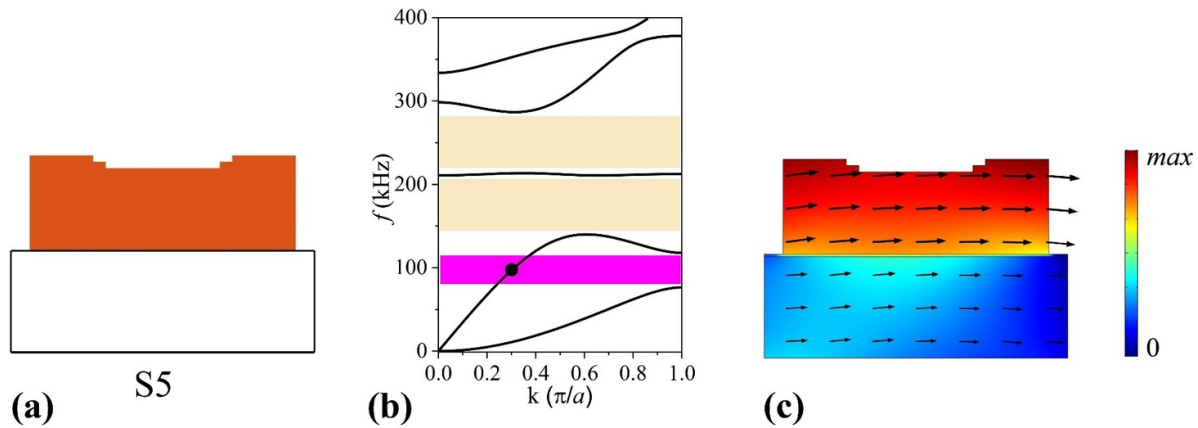


Figure 3. Optimization results for the widest single S0-mode band (objective 2). (a) The optimized structure. (b) the corresponding dispersion relations. The pink shadow area denotes the single-mode region. (c) A typical mode (100 kHz) within the single-mode band. The arrows indicate the displacement value and direction.

is obtained and shown in figure 3 which shows a broad S0-mode pass band in the range of 76.4~117.9 kHz. To illustrate the single-mode function of the designed MD, the mode at 100 kHz within this specific region is extracted and shown in figure 3(c), in which the colors and arrows denote the particle displacement value and direction, respectively. It is clear that the displacement in the plate is mainly polarized at the x direction, which corresponds to the S0-mode wave. Therefore, in this frequency region only S0-mode waves can propagate while the A0-mode waves are drastically filtered out.

3.3. Low-frequency filters

Targeting the low-frequency ultrasonic region, the MDs at subwavelength scale, i.e. the corresponding wavelengths are much larger than the geometric size of the design domain, are designed to offer the maximum bandgap widths. Two representative examples with customized dispersions below 30 kHz and 50 kHz are considered. For the first case, the evolution process is shown in figure 4(a), which, through demonstrating the generation details, leads to the finally optimized structure depicted in figure 4(b). It can be observed that the typical topology, consisting of a slim link and a large block, has already been formed at the very early stage of the evolution. The ‘mass-spring’ model is responsible for the subwavelength behavior which is typical of the well-known locally resonant effect. With the increasing iteration steps, this contrast is gradually enlarged to enhance the local resonance effect until the final convergence is reached. Performance-wise, two wide bandgaps are generated for the two cases as 18~30.4 kHz and 20~52.2 kHz respectively as illustrated in figures 4(b) and (c). Therefore, the proposed inverse design entails the proper structural topology to control the low-frequency guided waves by using the subwavelength-scale structures.

3.4. Mechanism explorations

The generation mechanisms of the broad bandgaps of the optimized structures are further explored. Examining figures 2 and 3 and table 2, three salient topological features can be

extracted. Firstly, a wide connection area between the added-on stubs and the plate is observed. Intuitively, the strong contact can enhance the coupling between the Lamb wave modes and stub modes. As a result, the bandgap originating from Bragg scattering is enlarged. Secondly, most structures possess a ‘trapezoid-like’ configurational feature. To explore the underlying physics, several modes corresponding to $B_1 \sim B_5$ in the dispersion curves in figure 2(c) are extracted and shown in figure 5, where the colors and arrows denote the particle displacement value and direction, respectively. Rotational modes are generally observed, which are responsible for the generation of the trapezoid-like structural shape. Meanwhile, the rotation modes, especially in $B_2 \sim B_4$, correspond to a flat band in the dispersion curves. This narrow pass band enlarges the bandgaps. Thirdly, the optimized configurations in all these cases are symmetric with respect to the horizontal direction due to the prescribed constraints. To characterize the vertical distribution of the microstructures, the centroids of the optimized structures, h_c , are calculated from

$$h_c = \frac{\sum_{i=1}^n (S_i \times h_i)}{\sum_{i=1}^n S_i} \quad (9)$$

where S_i and h_i respectively represent the area and centroid of the i th pixel filled with ‘solid’. The centroid of the entire structure can be derived by integrating the centroids of all solid pixels.

Figure 6 summarizes the relative centroid h_c/d of the added-on stubs in table 2, figures 2(b) and 3, which all exhibit Bragg scattering bandgaps. It is observed that all relative centroids locate at a close value around 0.4. This rather consistent phenomenon suggests that the centroid is a key inherent factor which affects the dispersion relations of the MDs.

Compared with the above Bragg scattering-type structures, the optimized structures S6 and S7 in figure 4 deliver low-frequency locally resonant bandgaps. First, the polarization directions of the plate mode are calculated as

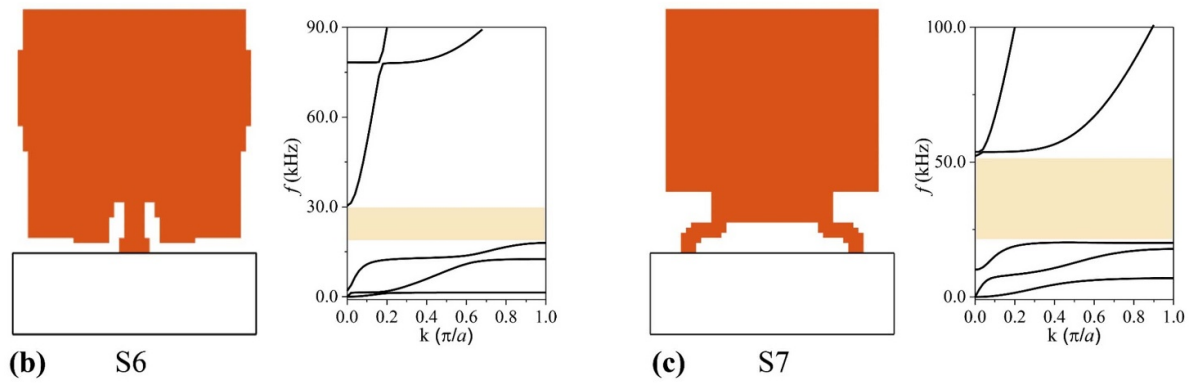
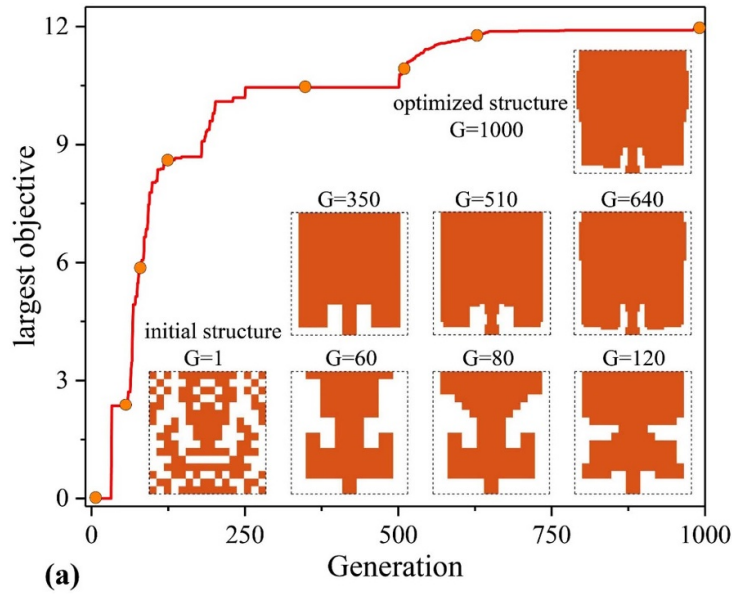


Figure 4. Optimization results aiming at the maximum bandgap widths in the low-frequency regions (objective 3). (a) Evolution histories of the optimized structures, (b) bandgaps below 30 kHz, (c) bandgaps below 50 kHz.

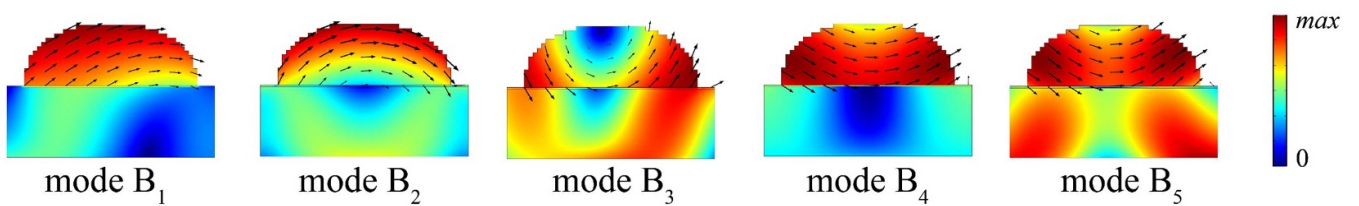


Figure 5. Several modes of the dispersion relations in figure 2(c).

$$\hat{u} = \frac{|\int u_i dv|}{\sqrt{(\int u_x dv)^2 + (\int u_y dv)^2}} \quad (10)$$

where \hat{u} represents the displacement polarization index of the modes; u_i ($i = x$ or y) denotes the directional displacement. Note that only the plate domain is taken into account in this calculation.

By using equation (10), the dispersion relations of the structure S6 are reconstructed and shown in figure 7(a), where the

curve color denotes the polarization direction. Three typical regions are observed. Apart from a bandgap region (Bandgap zone) marked in yellow, a y -direction polarized region (zone 1) and a x -direction polarized region (zone 2) appear. To further exploit this anisotropic property in the subwavelength scale, the effective mass density (EMD) based on the homogenization theory and defined in equation (11), is calculated numerically [25, 27] due to the complex configurations of the optimized structures. To this end, a harmonic perturbation excitation is applied to the left and right boundaries of the unit cell model

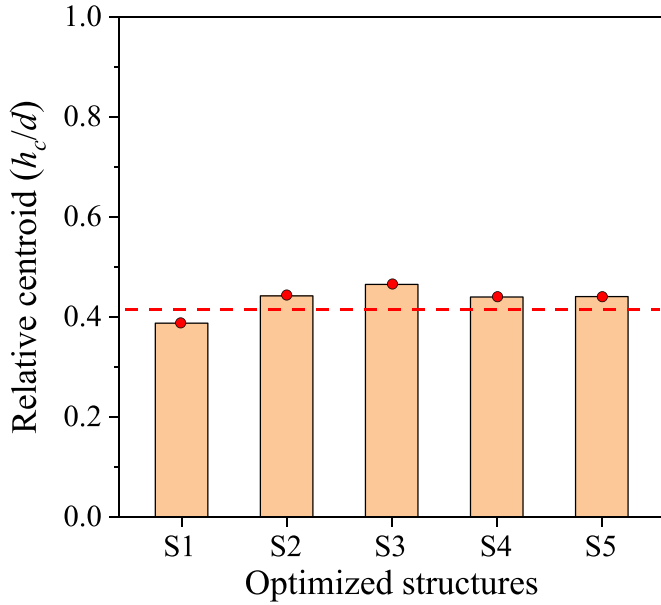


Figure 6. Relative centroids of the optimized structures.

in finite element simulations [27]. EMDs can be derived by extracting the averaged responses F_i ($i = x$ or y) on the boundaries as

$$\begin{pmatrix} F_x \\ F_y \end{pmatrix} = -\omega^2 V \begin{pmatrix} \rho_{11} & \rho_{12} \\ \rho_{21} & \rho_{22} \end{pmatrix}_{\text{eff}} \begin{pmatrix} U_x \\ U_y \end{pmatrix} \quad (11)$$

where F_i ($i = x$ or y) is the extracted forces on the boundaries of the unit cell; ω is the angular frequency; V represents the volume of the unit cell; $(\rho_{ij})_{\text{eff}}$ ($i, j = 1$ or 2) implies the effective EMD; U_i ($i = x$ or y) denotes the displacement applied to the boundaries of the unit cell.

Figure 7(b) shows the calculated EMD along x direction. It is relevant to note that the frequency ranges with negative EMDs not only include the bandgap range (Bandgap zone) but also cover the extra y -direction polarized regions (zone 1). This is because no x -direction mode exists in this single-mode band, which exhibits as an S0-mode wave bandgap. The modes C_1 and C_3 located in zone 1 clearly illustrate the polarized displacements of the plate, as shown in figure 7(d). Likewise, similar phenomenon also appears in the other direction. The negative EMD ranges of the y direction (figure 7(c)) agree with the sum of the bandgap region (Bandgap zone) and the x -direction polarized regions (zone 2). A wide polarized bandgap (18~76.7 kHz) which prohibits flexural waves is thus generated. The mode C_4 shown in figure 7(d) displays a typical x -polarized mode. In addition, localized displacements are observed in most modes where C_1 , C_2 and C_3 (below bandgap) mainly manifest stub modes while C_4 and C_5 (above bandgap) feature Lamb modes. The distinct contrast between these two types of modes favors the generation of the wide low-frequency bandgaps observed above. In summary, the optimized local-resonance type MDs not only possess broad bandgaps in the subwavelength scale, but also exhibit strong density anisotropy.

4. Validation of the designed wave filters

The performance of the optimized MDs is assessed from both numerical and experimental perspectives. The optimized structure in figure 2(b) is taken as a representative example to be discussed in detail hereafter. For conciseness, simulation/validation results and discussions of the other two types of MDs, respectively corresponding to the single-mode transmission filter in figure 3 and the low-frequency filter in figure 4(b), are put in appendix. It is worth noting that the optimized configuration in figure 2(b) is post-processed with smoothed edges to facilitate its fabrication as shown in figure 8(a). We verify that the dispersion property of the post-processed configuration is approximately the same as that of the original configuration in figure 2(c). Although the assumption of infinite periodicity was used to generate the dispersion curves, only a finite number of unit cells can be used in practice. The efficacy of the truncated practical MD is evaluated in the subsequent analyses.

4.1. Numerical validations

A finite element model is established with COMSOL Multiphysics 5.2a as shown in figure 8(b). Truthful to the common practice in SHM, a pair of piezoelectric transducers (PZTs) transducers are mounted on a 700 mm long and 2 mm thick aluminum plate. The sizes of the PZT actuator and sensor are 8 mm \times 0.3 mm and 5 mm \times 0.3 mm respectively. A five-cycle tone burst voltage excitation is applied to the PZT actuator with an amplitude of 200 V where three representative central frequencies are selected as 70 kHz, 220 kHz and 110 kHz respectively. 20 unit cells are used for the MD. Sensor responses are calculated/measured before and after the installation of the MD to show its effect, as presented in figure 9. For the 70 kHz excitation case (figure 9(a)) which falls into the pass band of the metamaterial assembly, both S0 and A0 waves can pass through the MD with slight wave attenuation. Under a 220 kHz excitation located in the stop band, however, Lamb waves are filtered out after the installation of the MD as shown in figure 9(b). For the last case at 110 kHz where only a single mode exists as informed by the dispersion relations, the S0 waves can pass through the MD while the A0 waves are significantly attenuated as shown in figure 9(c). To better visualize this, the wave fields at the 110 kHz are presented in figure 9(d) where the single S0-mode transmission behavior is clear by comparing the cases with and without the MD. It is relevant to note that a slight phase shift is caused by the MD in the temporal signals (figures 9(a)–(c)). This, however, does not affect the wave filtering function of the MD, as shown in figure 9, which is the main design objective. All these observations demonstrate that the performance of the designed MD serves the design purposes and is indeed governed by the engineered dispersion relations.

To further quantify the wave attenuation performance of the MD, frequency-domain analyses are also conducted to obtain the wave transmission spectra. Under a displacement perturbation excitation, the frequency is scanned within the 1~400 kHz range. A frequency response function ($FR = 20\log(u_1/u_0)$),

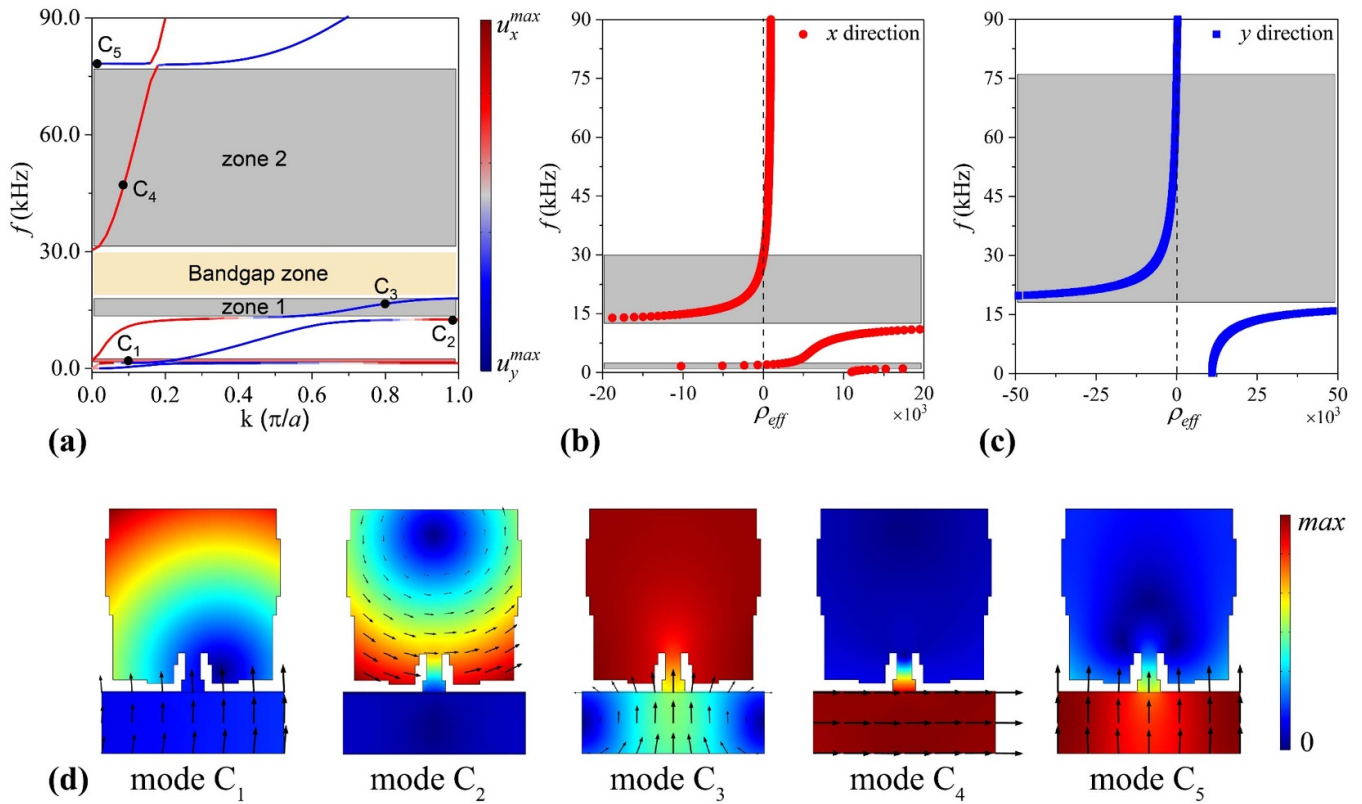


Figure 7. Mechanism analyses of the optimized structures in figure 4(b) based on effective material parameters. (a) Dispersion relations with colored polarization directions, effective mass density of (b) the x direction or (c) the y direction, (d) several representative modes.

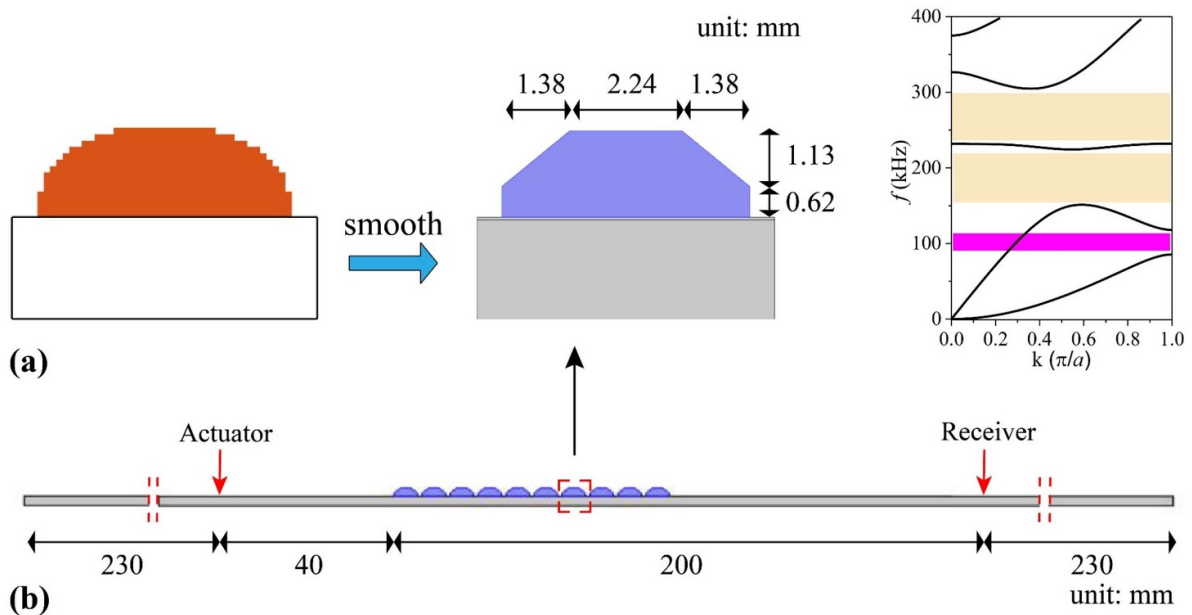


Figure 8. Simulation models. (a) The simplified structure, (b) the sketch of the transmission model with a finite number of unit cells.

where u_1 and u_0 are the displacement amplitudes of the receiver points with or without MDs, respectively), is defined to quantify the transmission ratio. Figure 10 depicts the frequency response results of S and A modes, respectively. In both S and A mode cases, significant attenuations, evidenced

by negative FR values, are observed within the bandgap frequency ranges. Moreover, in the frequency range around 86~116 kHz (shaded by a pink area in figure 10), the A mode wave (corresponding to a negative FR value) is attenuated while the S mode wave (corresponding to a nearly zero

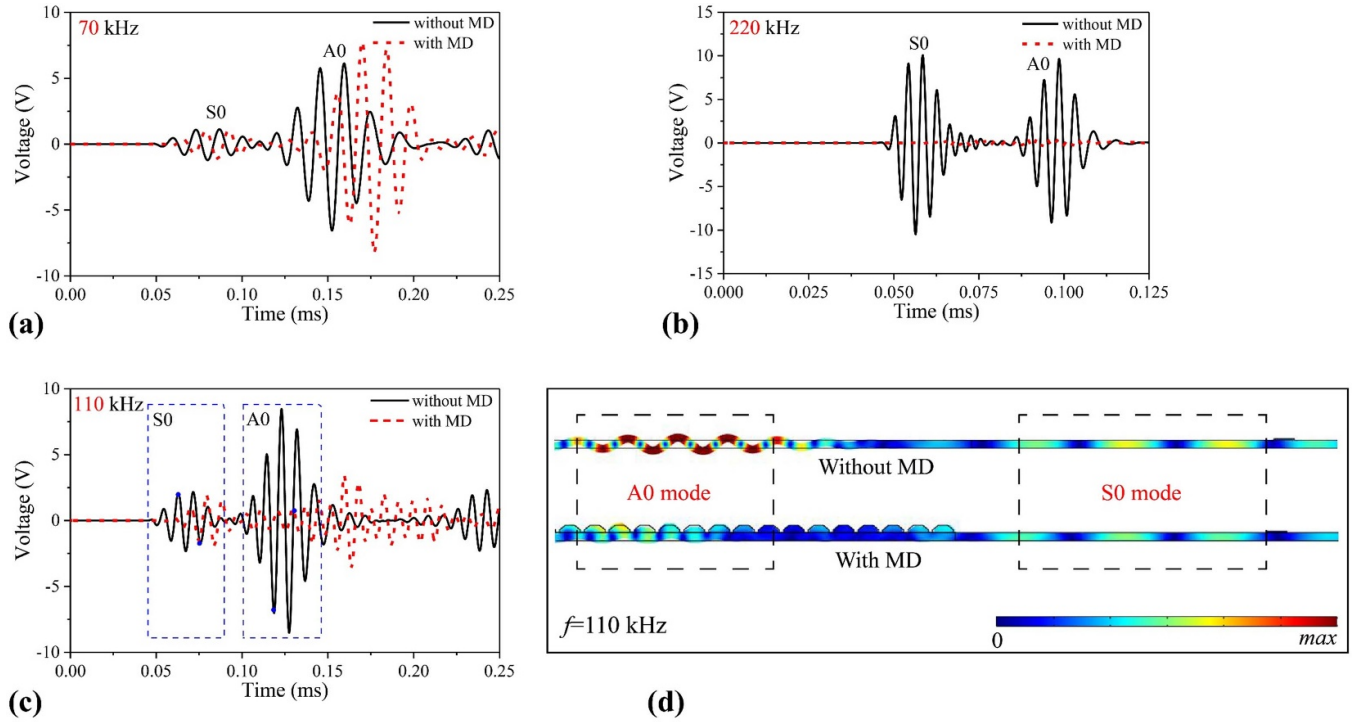


Figure 9. Simulated temporal signals under tone burst excitations with the central frequency of (a) 70 kHz in the pass band, (b) 220 kHz in the stop band and (c) 110 kHz in the single-mode band. (d) The wave fields under 110 kHz excitation with the MD ($t = 0.075$ ms) or without the MD ($t = 0.063$ ms).

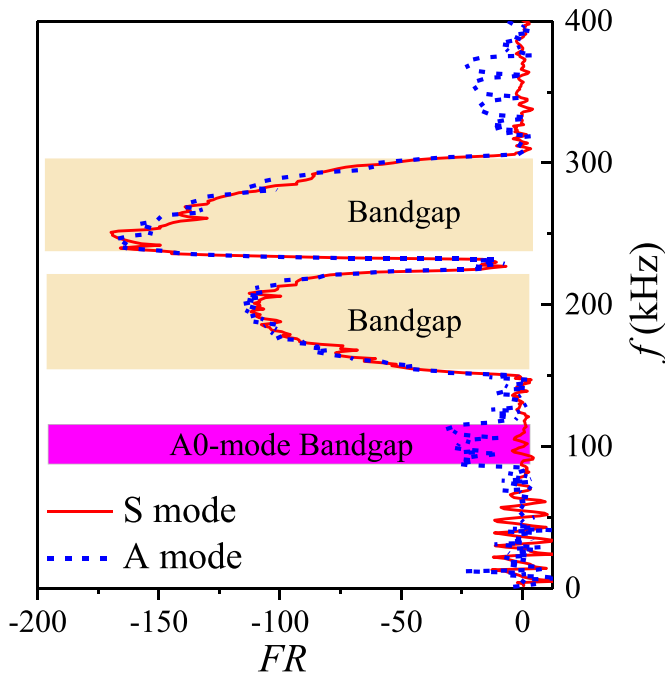


Figure 10. Frequency responses of respective S and A mode waves.

FR) is much less affected. Therefore, the stop band and the single-mode transmission band are proven to be in good agreement with the customized dispersion relations of the designed metamaterial assembly, evidenced by the above analyses from both time- and frequency-domain perspectives.

4.2. Experimental validations

Experiments are finally carried out to further evaluate the wave manipulation efficacy of the inverse-designed MD. In light of the relatively simple configuration of the designed added-on stubs, as shown in figure 8(a), mechanical cutting is used to fabricate the stub samples with 20 unit cells. The final size of all stubs is close to the one in figure 8(a) with roughly 0.1 mm manufacturing error (2% variation as compared with the numerically designed nominal width of the stub). This accuracy is deemed as acceptable, as evidenced by the subsequent results. In addition, the shape of the designed MDs is smoothed to facilitate the manufacturing (section 4.1), which can also be regarded as another geometric imperfection. Despite this, as shown in figure 8(a), the positions of the bandgaps of the simplified structure after post-processing remain basically the same as those of the originally optimized structure. Therefore, the manufacturing error, as well as some reasonable geometric imperfections, does not significantly affect the performance of the designed MDs. UHU epoxy glue is used to attach these stubs to the surface of a plate. The size of the plate is 700 mm \times 500 mm \times 2 mm while those of the PZT actuator and sensor are 8 mm \times 30 mm \times 0.3 mm and 5 mm \times 5 mm \times 0.3 mm, respectively. The location arrangement of the MD, the actuator and the sensor is identical to that in numerical simulations. Figure 11 shows the main experimental set-up alongside the connections among different measurement devices. The system works as follows: an excitation signal is first defined by the controller and generated by the National Instrument (NI) PXIe 5423 module. The

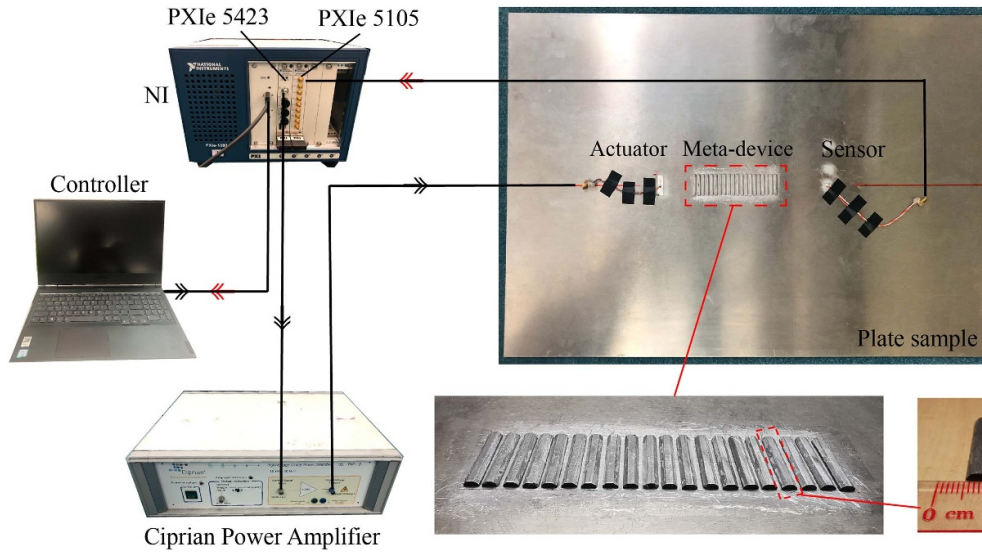


Figure 11. Experimental set-up.

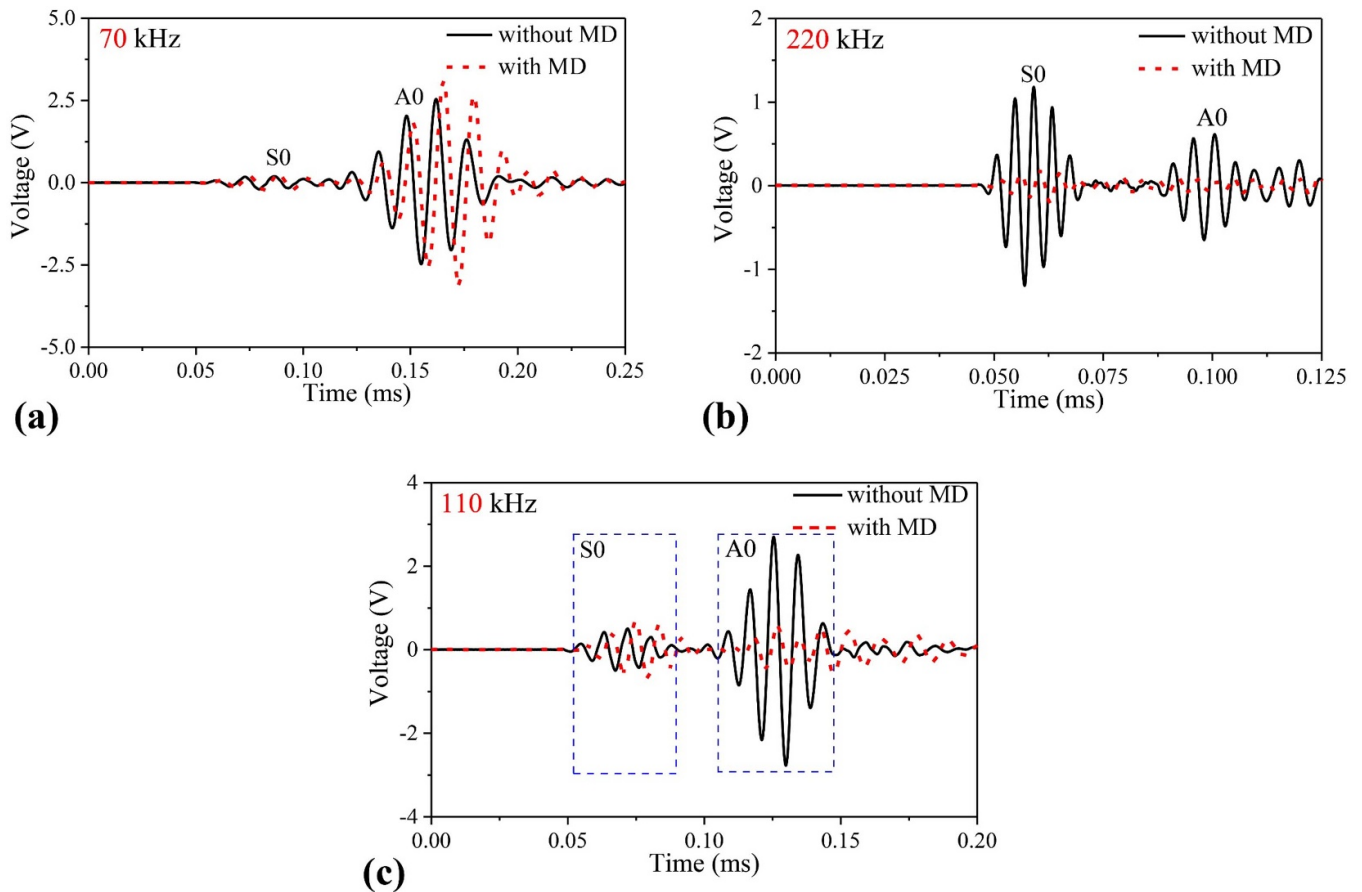


Figure 12. Experimental temporal signals under the tone burst excitations with the central frequency of (a) 70 kHz in the pass band, (b) 220 kHz in the stop band and (c) 110 kHz in the single-mode band.

output signal is then amplified by the Ciprian power amplifier and applied to the PZT actuator for the excitation of Lamb waves in the plate. The generated Lamb waves are finally captured by the PZT sensor and recorded with the NI PXIe 5105 module. The amplitude of the tone burst excitation

is set to 200 V with a sampling frequency of 10 MHz. For each test, 50 measurements are averaged to mitigate the influence of noise. At the same time, various imperfections of the experimental set-up might inevitably be encountered in practice. According to our numerical tests on some typical

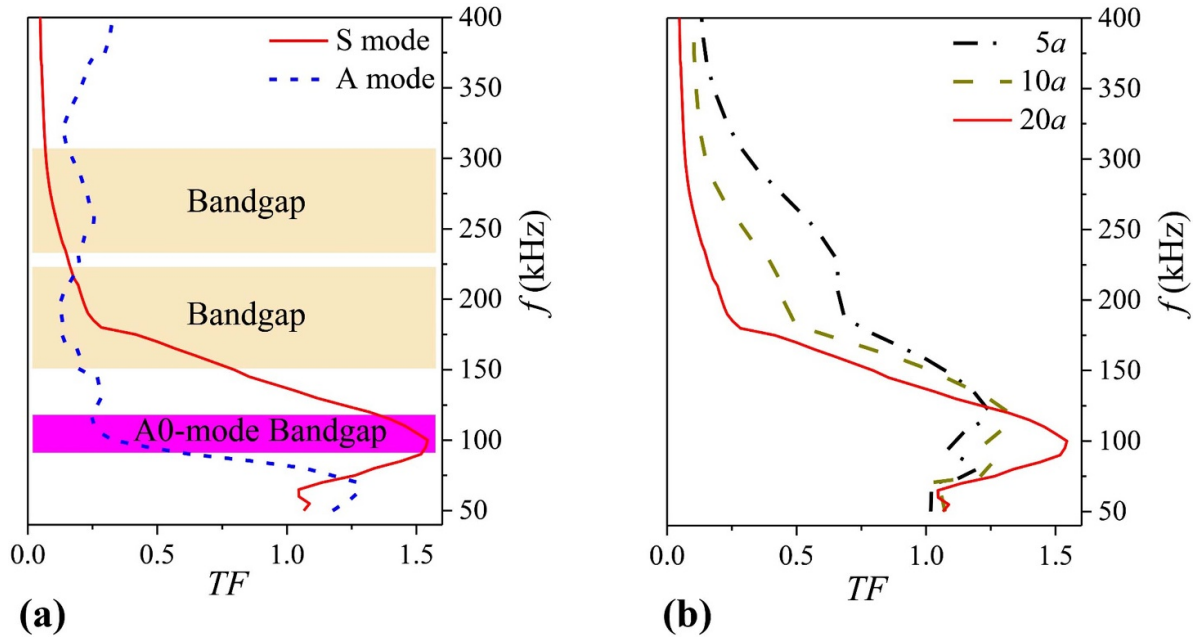


Figure 13. Experimentally measured wave attenuation. (a) The respective S or A mode transmission results, (b) the S mode transmission results respectively with 5, 10 or 20 unit cells.

imperfection factors (such as manufacturing imperfection of the stubs, imperfect periodic constants and imperfect bonding thickness) within a reasonable variation range, the bandgap positions of the designed MD are shown to basically remain stable. Detailed simulation results are, however, not given here. Therefore, for imperfections within a reasonable variation range, the optimized MDs show reasonable robustness in terms of bandgap generation and filtering performance, which can be considered as one of the advantages of the proposed MD design.

Same as the finite element validations, three typical responses are presented at 70 kHz, 220 kHz and 110 kHz respectively as shown in figure 12. As expected, both A0 and S0 waves can pass through the MD at 70 kHz in the pass band (figure 12(a)). The Lamb waves are significantly attenuated at 220 kHz in the stop band (figure 12(b)). Only S0 waves can pass through the MD at 110 kHz in the single-mode band. To obtain the frequency spectra of the individual S or A mode wave, the signals in the windows are respectively extracted. A transmission factor (TF) is defined to quantify the effect of the MD as

$$TF = \frac{CA_{MD}}{CA_{Intact}} \quad (12)$$

$$CA = \sqrt{\sum_{t=t_0}^{t_1} [A(t)]^2} \quad (13)$$

where CA represents the characteristic amplitude; t_0 and t_1 are the start and end time points of the windowed signals; $A(t)$ denotes the voltage value.

The TF results from 50 kHz to 400 kHz stepped by 5 kHz are calculated and presented in figure 13(a). Significant attenuations corresponding to small TF values are observed within the bandgap ranges. In the single-mode frequency range, S mode waves have large TF values, signifying effective energy passing, while A mode waves have small TF values evidencing effective energy prohibition. All these results again support the numerically predicted performance of the proposed MD.

Finally, the number of unit cells is varied (from 20, 10 to 5) to examine its impact on the transmission performance of the MD by gradually removing some stubs. Following the same procedure, the TFs for the different unit cell cases are measured and presented in figure 13(b). It can be noticed that the expected wave attenuation phenomenon is still pronounced even with five unit cells, which is gradually enhanced with an increasing number of periodicities. Nevertheless, the positions of the customized bands in different cases basically remain unchanged even when the number of unit cells changes.

5. Conclusions

Aiming at effective Lamb wave manipulation, especially in terms of wave frequency filtering and mode transmission, this work proposes a unified inverse strategy for MDs design. The MDs, taking the form of topologically designed lattices, are to be surface-mounted onto the host structure for the manipulation of guided Lamb waves. The three targeted wave manipulation functions include selective filtering of the wave frequency, single-mode transmission and low-frequency

subwavelength wave filtering. The unified inverse-design framework is based on topology optimization which delivers customized and broadband functional MDs. The mechanisms underpinning the achieved properties of the optimized structures are revealed. With an MD comprising a finite number of unit cells, time- and frequency-domain finite element simulations are conducted to validate the predefined wave functionalities, which are subsequently examined through experiments.

Broadband MDs are obtained by using the established design strategy. The strong contact/connection between the stubs and the plate, the trapezoid-like topology and specific structural centroid are identified as the salient topological features of the optimized MDs to generate broad Bragg scattering bandgaps. On the other hand, effective mass densities and directional polarizations explain the dispersion features of the local-resonance-type MDs in terms of the subwavelength bandgaps and single-mode band, where a strongly anisotropic density is observed. In both simulations and experiments, the broad bandgap feature and selective mode transmission are confirmed, which also agrees well with the dispersion relations.

This study provides a promising means to flexibly customize MDs for future guided wave manipulation. The designed MDs not only deliver multiple types of wave manipulation functions in a broadband range, but also possess a relatively simple topology, conducive to practical realization. This work hopefully offers new impetus to the exploration of metamaterials for SHM applications and paves the way forward for its practical implementation. Meanwhile, it is admitted that, as a proof-of-concept study, many issues need to be further considered, which also shows the limitations of the present work. For example, the efficacy of the designed MDs for enhancing damage diagnosis calls for further examination in the SHM context. In this regard, a three-dimensional model closer to practical SHM applications should be considered to assess the performance of the designed MDs. We believe the principles laid out in this paper are generic enough to be followed and extended to more complex cases or more diversified scenarios. While not being an issue for detection methods based on wave intensity such as amplitude, the phase lag and the time delay caused by MDs should be paid more attention for those SHM techniques based on temporal signal information, e.g. time-of-flight for damage localization. In principle, they can be characterized and calibrated when the MDs are designed and installed. Based on these information, suitable compensation methods can be developed to compensate for these adverse effects.

Data availability statement

The data that support the findings of this study are available upon reasonable request from the authors.

Acknowledgments

The work was supported by grants from the Research Grants Council of Hong Kong Special Administrative Region (PolyU 152013/21E), the National Natural Science Foundations of China through SHENG project (Polish-Chinese Funding Initiative, 51961135302), Research Fund of State Key Laboratory of Mechanics and Control of Mechanical Structures (Nanjing University of Aeronautics and Astronautics, China. Grant No. MCMS-E-0520K01), the Natural Science Foundation of Shanghai (22ZR1462700), the Fundamental Research Funds for the Central Universities and the Innovation and Technology Commission of the HKSAR Government to the Hong Kong Branch of National Rail Transit Electrification and Automation Engineering Technology Research Center.

Appendix. Validation and discussions on single-mode transmission and low-frequency filtering

Finite element simulations are used to assess the wave filtering performance of the designed structures in figure 3 in terms of single-mode transmission and in figure 4(b) for low-frequency filtering, respectively. By using the simulation model in figure 8(b) with 20 unit cells, frequency-domain analyses are conducted to obtain the wave transmission spectra. As shown in figure A1(a), two wave attenuation zones, 140~211 kHz and 213~286 kHz, are observed for both A and S modes, which correspond to the bandgaps in the dispersion curves; In the range of 76~118 kHz marked by the shaded pink area, only the S mode waves can pass while the A mode waves are filtered out, thus featuring an A-mode bandgap. As to figure A1(b) showing the achieved low-frequency filtering capability of the MD, the attenuation zone of the S mode waves is the sum of the bandgap zone and zone 1 while that of the A mode waves is the sum of the bandgap zone and zone 2. Zone 1 with y -direction polarized mode acts as an S-mode filter while zone 2 with x -direction polarized mode as an A-mode filter. In summary, all attenuation zones identified from the wave transmission calculation results are in good agreement with the predicted dispersion features in terms of frequency ranges, which confirm the respective wave filtering functionalities for which the MDs are designed.

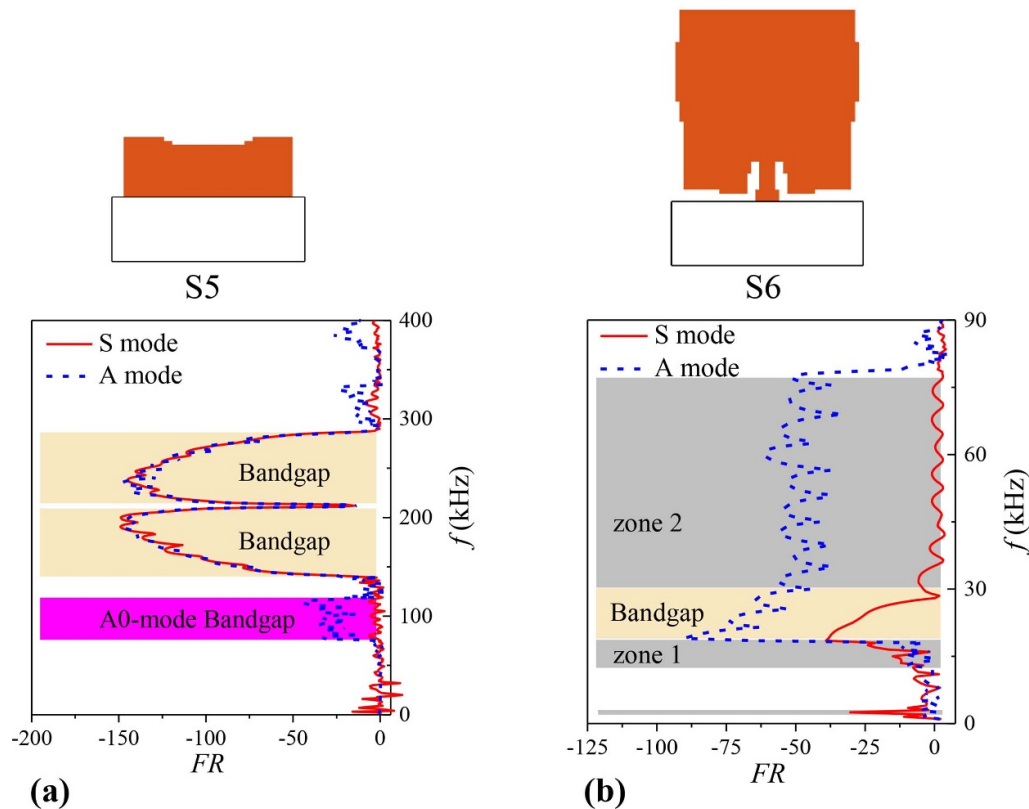


Figure A1. Frequency responses in simulations. (a) The single-mode transmission filter in figure 3, (b) the low-frequency filter in figure 4(b).

ORCID iDs

Ze Liu <https://orcid.org/0000-0002-4565-4767>

Sheng-Bo Shan <https://orcid.org/0000-0002-0950-6193>

Li Cheng <https://orcid.org/0000-0001-6110-8099>

References

- [1] Giurgiutiu V 2007 *Structural Health Monitoring: With Piezoelectric Wafer Active Sensors* (Amsterdam: Elsevier)
- [2] Chang F K, Markmiller J F C, Yang J and Kim Y 2001 *Structural health monitoring System Health Management: With Aerospace Applications* (New York: Wiley) pp 419–28
- [3] Cantrell J H 2009 Nonlinear dislocation dynamics at ultrasonic frequencies *J. Appl. Phys.* **105** 043520
- [4] Xiang Y, Deng M and Xuan F-Z 2014 Creep damage characterization using nonlinear ultrasonic guided wave method: a mesoscale model *J. Appl. Phys.* **115** 044914
- [5] Chen Z and Qu J 2013 Dislocation-induced acoustic nonlinearity parameter in crystalline solids *J. Appl. Phys.* **114** 164906
- [6] Chillara V K and Lissenden C J 2015 Review of nonlinear ultrasonic guided wave nondestructive evaluation: theory, numerics, and experiments *Opt. Eng.* **55** 011002
- [7] Shan S, Cheng L and Li P 2016 Adhesive nonlinearity in Lamb-wave-based structural health monitoring systems *Smart Mater. Struct.* **26** 025019
- [8] Shan S, Cheng L and Wen F 2018 Design of nonlinear-Lamb-wave-based structural health monitoring systems with mitigated adhesive nonlinearity *Smart Mater. Struct.* **27** 105006
- [9] Wen F, Shan S, Radecki R, Staszewski W J and Cheng L 2021 Shear-lag modelling of surface-bonded magnetostrictive transducers for shear horizontal wave generation in a non-ferromagnetic plate *Smart Mater. Struct.* **30** 035026
- [10] Shan S and Cheng L 2022 Two-dimensional scattering features of the mixed second harmonic A0 mode Lamb waves for incipient damage localization *Ultrasonics* **119** 106554
- [11] Kumar S, Bhushan P, Prakash O and Bhattacharya S 2018 Double negative acoustic metastructure for attenuation of acoustic emissions *Appl. Phys. Lett.* **112** 101905
- [12] Liu Z, Qin K-Q and Yu G-L 2020 Partially embedded gradient metabarrier: broadband shielding from seismic Rayleigh waves at ultralow frequencies *J. Eng. Mech.* **146** 04020032
- [13] Dong H-W, Zhao S-D, Wei P, Cheng L, Wang Y-S and Zhang C 2019 Systematic design and realization of double-negative acoustic metamaterials by topology optimization *Acta Mater.* **172** 102–20
- [14] Dong H-W, Zhao S-D, Wang Y-S, Cheng L and Zhang C 2020 Robust 2D/3D multi-polar acoustic metamaterials with broadband double negativity *J. Mech. Phys. Solids* **137** 103889
- [15] Pendry J B 2000 Negative refraction makes a perfect lens *Phys. Rev. Lett.* **85** 3966
- [16] Dong H-W, Zhao S-D, Wang Y-S and Zhang C 2017 Topology optimization of anisotropic broadband double-negative elastic metamaterials *J. Mech. Phys. Solids* **105** 54–80
- [17] Nassar H, Xu X C, Norris A N and Huang G L 2017 Modulated phononic crystals: non-reciprocal wave propagation and Willis materials *J. Mech. Phys. Solids* **101** 10–29
- [18] Li P and Biwa S 2019 The SH0 wave manipulation in graded stubbed plates and its application to wave focusing and frequency separation *Smart Mater. Struct.* **28** 115004

- [19] Shen H, Paidoussis M P, Wen J, Yu D, Cai L and Wen X 2012 Acoustic cloak/anti-cloak device with realizable passive/active metamaterials *J. Phys. D: Appl. Phys.* **45** 285401
- [20] Liu Z, Zhang X, Mao Y, Zhu Y Y, Yang Z, Chan C T and Sheng P 2000 Locally resonant sonic materials *Science* **289** 1734–6
- [21] D'Alessandro L, Belloni E, Ardito R, Corigliano A and Braghin F 2016 Modeling and experimental verification of an ultra-wide bandgap in 3D phononic crystal *Appl. Phys. Lett.* **109** 221907
- [22] Lucklum F and Vellekoop M J 2018 Bandgap engineering of three-dimensional phononic crystals in a simple cubic lattice *Appl. Phys. Lett.* **113** 201902
- [23] Liu Z, Dong H-W and Yu G-L 2021 Topology optimization of periodic barriers for surface waves *Struct. Multidiscipl. Optim.* **63** 463–78
- [24] Zeng Y, Zhang S-Y, Zhou H-T, Wang Y-F, Cao L, Zhu Y, Du Q-J, Badreddine Assouar M and Wang Y-S 2021 Broadband inverted T-shaped seismic metamaterial *Mater. Des.* **208** 109906
- [25] Oudich M, Djafari-Rouhani B, Pennec Y, Assouar M B and Bonello B 2014 Negative effective mass density of acoustic metamaterial plate decorated with low frequency resonant pillars *J. Appl. Phys.* **116** 184504
- [26] Badreddine Assouar M and Oudich M 2012 Enlargement of a locally resonant sonic band gap by using double-sides stubbed phononic plates *Appl. Phys. Lett.* **100** 123506
- [27] Zhu R, Liu X N, Huang G L, Huang H H and Sun C T 2012 Microstructural design and experimental validation of elastic metamaterial plates with anisotropic mass density *Phys. Rev. B* **86** 144307
- [28] Miniaci M, Gliozzi A S, Morvan B, Krushynska A, Bosia F, Scalerandi M and Pugno N M 2017 Proof of concept for an ultrasensitive technique to detect and localize sources of elastic nonlinearity using phononic crystals *Phys. Rev. Lett.* **118** 214301
- [29] Tian Y, Shen Y, Rao D and Xu W 2019 Metamaterial improved nonlinear ultrasonics for fatigue damage detection *Smart Mater. Struct.* **28** 075038
- [30] Tian Y and Shen Y 2020 Selective guided wave mode transmission enabled by elastic metamaterials *J. Sound Vib.* **485** 115566
- [31] Shan S, Wen F and Cheng L 2021 Purified nonlinear guided waves through a metamaterial filter for inspection of material microstructural changes *Smart Mater. Struct.* **30** 095017
- [32] Yang Y, Ng C T, Kotousov A, Sohn H and Lim H J 2018 Second harmonic generation at fatigue cracks by low-frequency Lamb waves: experimental and numerical studies *Mech. Syst. Signal Process.* **99** 760–73
- [33] Holland J H 1975 *Adaptation in Natural and Artificial Systems* (Ann Arbor, MI: University of Michigan Press)
- [34] Dong H-W, Su X-X, Wang Y-S and Zhang C 2014 Topological optimization of two-dimensional phononic crystals based on the finite element method and genetic algorithm *Struct. Multidiscipl. Optim.* **50** 593–604
- [35] Wan X, Tse P W, Xu G H, Tao T F and Zhang Q 2016 Analytical and numerical studies of approximate phase velocity matching based nonlinear S0 mode Lamb waves for the detection of evenly distributed microstructural changes *Smart Mater. Struct.* **25** 045023
- [36] Shan S, Cheng L and Wen F 2018 Characterization of nonplanar second harmonic Lamb waves with a refined nonlinear parameter *J. Nondestruct. Eval. Diagn. Prognost. Eng. Syst.* **1** 011004